

Gas phase vibrational spectroscopy of mass-selected vanadium oxide anions†

Gabriele Santambrogio,^a Mathias Brümmer,^a Ludger Wöste,^a Jens Döbler,^b Marek Sierka,^b Joachim Sauer,^{*b} Gerard Meijer^c and Knut R. Asmis^{*c}

Received 28th February 2008, Accepted 10th April 2008

First published as an Advance Article on the web 28th May 2008

DOI: 10.1039/b803492c

The vibrational spectra of vanadium oxide anions ranging from $V_2O_6^-$ to $V_8O_{20}^-$ are studied in the region from 555 to 1670 cm^{-1} by infrared multiple photon photodissociation (IRMPD) spectroscopy. The cluster structures are assigned and structural trends identified by comparison of the experimental IRMPD spectra with simulated linear IR absorption spectra derived from density functional calculations, aided by energy calculations at higher levels of theory. Overall, the IR absorption of the $V_mO_n^-$ clusters can be grouped in three spectral regions. The transitions of (i) superoxo, (ii) vanadyl and (iii) V–O–V and V–O• single bond modes are found at ~ 1100 cm^{-1} , 1020 to 870 cm^{-1} , and 950 to 580 cm^{-1} , respectively. A structural transition from open structures, including at least one vanadium atom forming two vanadyl bonds, to caged structures, with only one vanadyl bond per vanadium atom, is observed in-between tri- and tetravanadium oxide anions. Both the closed shell $(V_2O_5)_{2,3}VO_3^-$ and open shell $(V_2O_5)_{2,4}^-$ anions prefer cage-like structures. The $(V_2O_5)_{3,4}^-$ anions have symmetry-broken minimum energy structures (C_s) connected by low-energy transition structures of C_{2v} symmetry. These double well potentials for V–O–V modes lead to IR transitions substantially red-shifted from their harmonic values. For the oxygen rich clusters, the IRMPD spectra prove the presence of a superoxo group in $V_2O_7^-$, but the absence of the expected peroxy group in $V_4O_{11}^-$. For $V_4O_{11}^-$, use of a genetic algorithm was necessary for finding a non-intuitive energy minimum structure with sufficient agreement between experiment and theory.

Introduction

Transition metal oxides are interesting materials due to their structural variability and redox activity. Vanadium oxides, in particular, are found in such diverse applications as supported catalysts,¹ cathode materials in lithium batteries,² bolometric detectors³ and spintronic devices.⁴ One of the most intriguing aspects is the change of structure and properties as a function of the aggregation level such as bulk crystals, thin films, nanotubes as well as nano-sized and subnano-sized clusters. In the important area of supported transition metal oxide catalysts,⁵ neither the size and distribution of the active particles on the support surface, nor their structure are

sufficiently known. While some progress has been made to mass-selectively deposit and characterize supported clusters,⁶ the interpretation of these experiments remains complex. It therefore proves useful to study the size-dependent properties of transition metal oxide clusters under well-controlled conditions in the gas phase, *i.e.* in the absence of any interactions with a medium or support.⁷

One of the first experimental gas phase studies on negative ions of vanadium oxide clusters was performed by Rudnyi *et al.*,⁸ who unexpectedly detected VO_2^- , VO_3^- , $V_2O_5^-$, $V_3O_8^-$ and $V_4O_{10}^-$ in the vapor of vanadium oxide at temperatures of 1200–1500 K, hinting at a particular high stability of these vanadium oxide anions towards dissociation as well as electron detachment. Collision induced dissociation studies⁹ supported these results. In general, dissociation rather than electron detachment was observed. Whereas the same building blocks (VO_2 , VO_3 , and V_2O_5) were found as before for the respective cations, the average oxygen content was higher and evidence was presented for higher adsorption energies for molecular oxygen in the negative ions. The reactivity of smaller $V_mO_n^-$ clusters towards carboxylic acid esters,¹⁰ hydrocarbons¹¹ and, more recently, alcohols¹² was studied (see ref. 13 and references therein for a summary of reactivity studies on cationic and neutral V_mO_n clusters) and a decreasing reactivity with cluster size was found. In particular, $V_3O_8^-$ and $V_4O_{10}^-$ did not react, indicating particularly stable structures containing fully coordinated V atoms. Anion

^a Institut für Experimentalphysik, Freie Universität Berlin, Arnimallee 14, D-14195 Berlin, Germany

^b Institut für Chemie, Humboldt-Universität Berlin, Unter den Linden 6, D-10099 Berlin, Germany. E-mail: js@chemie.hu-berlin.de

^c Fritz-Haber-Institut der Max-Planck-Gesellschaft, Faradayweg 4-6, D-14195 Berlin, Germany. E-mail: asmis@fht-berlin.mpg.de

† Electronic supplementary information (ESI) available: Total B3LYP/TZVP energies (Table S1); Scaled harmonic vibrational frequencies, relative intensities and mode assignment for additional isomers of vanadium oxide anions from B3LYP/TZVP calculations (Table S2); DFT energy as a function of the difference of the two V–O distances in the V–O–V bridge (Table S3); DFT results for the minimum and saddle point structures as well as potential parameters of the quartic and Manning-type potentials for $V_6O_{15}^-$ and $V_8O_{20}^-$ (Table S4); eigenvalues and eigenfunctions of the double-well potential (Fig. S1). See DOI: 10.1039/b803492c

photoelectron spectroscopy^{14,15} has been used to measure electron detachment energies of mono- and divanadium oxide anions. Some of the oxygen-rich $V_mO_n^-$ clusters were found to have exceptionally high electron affinities (>5 eV). Vyboishchikov and Sauer¹⁶ were the first to characterize the structure and detachment energies of smaller $V_mO_n^-$ anions (up to $m = 4$ and $n = 11$) employing density functional theory (DFT).

Information on the structure of the gas phase ions is difficult to get experimentally. Trapped ion electron diffraction¹⁷ has been successfully applied to large silver and gold clusters (see ref. 18 and references therein), but has not been extended to metal oxide clusters yet. Here, we examine the vibrational spectra of $V_mO_n^-$ clusters ranging from $V_2O_6^-$ to $V_8O_{20}^-$ by mass-selective infrared multiple photon photodissociation (IRMPD) spectroscopy,^{19–21} which is currently one of the most sensitive, generally applicable structural characterization approaches for cluster ions. The low number densities in the gas phase require intense and tunable IR radiation in the fingerprint region of metal oxide clusters,²² *i.e.*, the region from 500 to 1600 cm^{-1} , which is provided by a free electron laser.²³ Structure determination is indirect. The observed spectra are compared with spectra predicted by DFT for energy minimum structures and, in special cases, for low-energy transition state structures.

Three types of vanadium oxide anions are studied. The open-shell $(V_2O_5)_n^-$ anions are closely related to the neutral $(V_2O_5)_n$ clusters, which represent the gas phase analogs of the crystalline phase of V_2O_5 in which vanadium is in its highest (+V) oxidation state. In the corresponding anions the electron added to these clusters will occupy vanadium 3d states and its effect on the cluster structure is size-dependent.²⁴ It localizes at one vanadium site in the $n = 3, 4$ anions, whereas it delocalizes in the $n = 2$ anion, keeping the full fourfold symmetry of the corresponding neutral V_4O_{10} cluster. To form fully oxidized, closed shell anions, a VO_3^- unit is needed, resulting in clusters of the type $(V_2O_5)_nVO_3^-$. We will show that both the $(V_2O_5)_{2,3}VO_3^-$ and $(V_2O_5)_{2-4}^-$ anions form stable cage-like structures that fundamentally differ from the layered structure of the crystal. For $V_4O_{10}^-$ and $(V_2O_5)_{2-4}^-$ such structures^{16,25} had been predicted before by DFT. The oxygen rich clusters, $V_2O_6^-$, $V_2O_7^-$, and $V_4O_{11}^-$, are of interest because their neutral counterparts may contain superoxo and peroxo species (formally O_2^- and O_2^{2-} instead of O^{2-}) that may play a role in the re-oxidation of reduced vanadium oxide sites²⁶ on the surface of supported vanadium oxide catalysts. However, as we will show, the extra electron that is needed to turn the neutral V_4O_{11} cluster into the $V_4O_{11}^-$ cluster anion prevents the existence of peroxo groups.

A communication reporting preliminary results on the experimental and calculated IR spectra of $V_4O_{10}^-$, $V_6O_{15}^-$ and $V_8O_{20}^-$ was previously published²⁴ and mainly focussed on the reliability of DFT functionals to correctly describe electron delocalization in these systems. In a separate study, the effects of oxygen deficiency and addition of methyl groups on the $V_4O_{10}^-$ core have been studied by IRMPD spectroscopy of vanadium oxide containing ions from an ion spray source.²⁷ Reference to the results of the present original article has been made in two review papers,^{19,22} which included overview figures (Fig. 4, 6 and 16 of ref. 22 and Fig. 11 and

13 of ref. 19) summarizing the experimental and some of the computational data. Here, we present the first complete report on this study and discuss the procedure of how we arrive at the assigned structures. In particular, we give the first detailed description of both, the experimental and calculated IR spectra, including measured IR band positions for different fragment ions, calculated dissociation energies and electron affinities, as well as simulated IR spectra for ground, as well as energetically higher lying isomers. We also report coupled cluster results for the relative stability of different isomers and compare them with B3LYP predictions.

Experimental

The experiments were carried out on a previously described tandem mass spectrometer–ion trap system,²⁸ which was temporarily installed at the “Free Electron Laser for Infrared eXperiments” (FELIX) user facility²⁹ of the FOM Institute Rijnhuizen (The Netherlands). Briefly, $V_mO_n^-$ clusters are prepared by a pulsed laser vaporization source. The second harmonic of a Nd:YAG laser (Quantel Brilliant Ultra, 532 nm, 8 ns, ~ 10 mJ pulse⁻¹), operated at 20 Hz, is focused on a translating and rotating vanadium rod (Alfa Aesar, 99.5% purity). The plasma containing vanadium atoms are entrained in a pulse of 1.5% O_2 seeded in He carrier gas, expanded through a clustering channel and passed through a 2 mm diameter skimmer. The beam of negative ions is collimated in a radio frequency (RF) decapole ion guide. The ion guide is filled with argon in order to compress the ion phase space distribution and to thermalize the internal degrees to room temperature through many collisions with the buffer gas atoms. The ions are then guided into the first RF quadrupole mass filter, which is typically operated at unit resolution. Mass-selected cluster ions are directed into a cooled, He-filled (~ 0.02 mbar), RF hexadecapole ion trap, where they are accumulated and thermalized close to ambient temperature (~ 16 K) through inelastic collisions with the He buffer gas.

IR photodissociation spectra are obtained by photoexcitation of the trapped ions with pulsed radiation from FELIX, which is operated at 5 Hz and applied collinearly to the ion trap main axis. A measurement cycle is initiated by the trigger signal of the previous FELIX pulse and the ion trap is filled with mass-selected ions for a fixed time t_{fill} . After entering the ion trap region the ions are cooled, which is assumed to proceed on a time scale of up to a few milliseconds. Directly after FELIX fires, the ions are extracted from the ion trap and the mass-selected ion yield is monitored. This cycle is repeated multiple times and then FELIX is set to the next wavelength. In order to check the stability of the source conditions, the parent ion yield is measured once at the beginning and once at the end of each wavelength step. Its variations are typically on the order of 10%.

When the FELIX macropulse intensity is high enough, multiple IR photons can be absorbed; the cluster is heated and eventually, when sufficient energy has been deposited into the system, either dissociates, producing ionic and neutral photofragments, or undergoes electron detachment, producing

neutral products. The present conditions, *i.e.*, the characteristic macro pulse structure of FELIX (a 5 μs macropulse is composed of five thousand 1 ps micropulses spaced by 1 ns), favor a sequential and incoherent *multiple photon* absorption mechanism,^{21,30} rather than coherent *multiphoton* absorption. In this picture, photons will only be absorbed by the initially vibrationally cold cluster ions, if the wavelength is resonant with a fundamental vibrational transition. However, absorption of all photons in only a single vibrational ladder is unrealistic at moderate laser intensities. Rather, the absorbed energy diffuses, due to anharmonic coupling, over the bath of vibrational background states, effectively de-exciting the bright vibrational transition before the next micropulse arrives. At high laser fluence (and low density of states) the probability of multiphoton transitions as well as directly exciting overtones is enhanced,³¹ complicating the interpretation of the IRMPD spectra. Under the present experimental conditions, V_2O_6^- was the smallest cluster for which we could detect fragment ions. The fragment ion yield was less than 5% of the parent yield for the smaller anions, and increased with cluster size up to more than 80% for $\text{V}_8\text{O}_{20}^-$, the largest cluster studied.

Ideally, with t_{fill} less than 200 ms, the experiment can make use of the full FELIX repetition rate of 5 Hz. In practice, longer filling times sometimes proved to yield a superior ratio between signal statistics and acquisition time; filling times between 150 to 350 ms are used throughout the experiments described here. Note, for fill times larger than 200 ms some trapped ions experience multiple FELIX macropulses. Generally, an overview spectrum is first measured in the region from 6 up to 18 μm with a step size of 0.1 μm . Then, the possible fragment channels are determined by measuring an “on-resonance” fragment ion mass spectrum with FELIX tuned to the vanadyl absorption band at ~ 10 μm and scanning the second mass filter. Spectra with smaller step sizes and longer accumulation times are then measured for the fragment ions of interest. During one spectral scan, up to four ions of different mass are monitored. The output of FELIX is introduced into the ion trap region through a coated ZnSe window, a 48 cm focal length KBr lens and a 5 mm thick KBr window. Focusing of the FELIX beam is required to avoid light scattering off the ion trap exit and entrance lenses. The transmission efficiency of the KBr optics is $>85\%$ between 3 and 20 μm , while the efficiency of the coated ZnSe window is $>85\%$ between 8 and 15 μm and about 50% at 6 and 17 μm . The experiments on the larger cluster ions were performed using a KRS-5 window instead of the ZnSe window. Its transmission (70–75%) is lower than that of ZnSe, but considerably less dependent on wavelength near the edges of the region studied here. All IRMPD spectra shown here were not corrected for this transmission dependence, because this would require the knowledge of the cross sections of the individual absorption steps comprising the sequential multiple photon absorption process. In the present experiments, the FELIX bandwidth (RMS) varied from 0.3 to 0.5% of the central wavelength and the pulse energies ranged from 30–60 mJ per macropulse, measured before the ZnSe and KBr optics. The accuracy of the determined vibrational frequencies is generally within 1% of the central wavelength.

Computational methods

The DFT calculations use the TURBOMOLE program.³² The B3LYP hybrid functional³³ is employed. The TZVP basis sets applied are the triple-zeta valence basis sets developed by Ahlrichs and coworkers³⁴ augmented by polarization functions, a d-set for oxygen and a p-set for vanadium.³⁵ Structure optimizations use tight convergence criteria. Structures are optimized until Cartesian gradients are smaller than $1 \times 10^{-4} E_{\text{h}} a_0^{-1}$ and the energy change is smaller than $1 \times 10^{-6} E_{\text{h}}$ (see ESI for absolute energies).† The SCF convergence criterion is $1 \times 10^{-7} E_{\text{h}}$ for the energy and 1×10^{-7} a.u. for the root mean square of the density. Harmonic vibrational frequencies are obtained from second analytic derivatives.³⁶ It is known that B3LYP vibrational frequencies are systematically too large (see, *e.g.*, ref. 37) and, therefore, agreement with observed frequencies can be improved by scaling. Scaling accounts of both anharmonicities and systematic errors of the calculated harmonic force constants (calculated harmonic wave numbers are compared to observed fundamentals including anharmonicities). We use scaling parameters,³⁸ that we determined for small vanadium oxide cluster cations. Vanadyl, peroxy and superoxy modes are scaled by 0.9167 and all V–O–V modes by 0.9832.

The global optimizations of $\text{V}_4\text{O}_{11}^-$ structures use an implementation³⁹ of the genetic algorithm that closely follows the ideas of Daeven and Ho.⁴⁰ A population of 16 structures has been used. In each of the 40 generations 8 child structures have been optimized by B3LYP using the smaller SVP basis set. The lowest energy structures emerging have been re-optimized with B3LYP/TZVP.

There are several V_mO_n^- anions for which B3LYP yields small stability differences between the lowest energy structures (V_2O_6^- , $\text{V}_4\text{O}_{11}^-$, $\text{V}_5\text{O}_{13}^-$) or for which B3LYP and B3LYP yield conflicting results ($\text{V}_4\text{O}_{10}^-$ and $\text{V}_6\text{O}_{15}^-$). In these cases, we have checked the performance of TZVP in DFT calculations by comparing with B3LYP calculations using the larger def2-TZVP basis set [6s4p4d1f]/[5s3p2d1f].⁴¹ The energy differences between optimized structures of the two lowest energy isomers are smaller than 2.5 kJ mol⁻¹ in all cases (see Table 5 below), indicating that the TZVP basis set is sufficient for systems without and with occupied d-states. In addition, explicit electron correlation calculations have been made with CCSD(T). The TZVP basis set used is far from yielding converged results; nevertheless it provides further support for the reliability of the predicted stability sequences. Coupled cluster calculations with single and double substitutions and perturbative treatment of triple substitutions, CCSD(T),⁴² are made with MOLPRO 2002.6.⁴³ The open-shell calculations use a restricted Hartree–Fock (ROHF) reference and were performed in the frame of restricted coupled cluster RCCSD(T).⁴⁴ The TZVP basis set is adopted and only the valence electrons are correlated (3d and 4s for vanadium). For the CCSD(T) structure optimization on V_2O_6^- isomers, analytical UCCSD(T) gradients (ROHF reference function)⁴⁵ have been used as implemented in ACES II.⁴⁶

For two cases ($\text{V}_6\text{O}_{15}^-$ and $\text{V}_8\text{O}_{20}^-$) we went beyond the harmonic approximation and solved the one-dimensional vibrational eigenvalue problem for the symmetric double-well

potential connecting the saddle point C_{2v} structure with the two equivalent C_s minimum structures. The potential was approximated by a 16th-degree polynomial function, which was fit to 21 points of the relaxed DFT potential energy curve. The simplest analytical expression for a symmetric double-well potential, the quartic polynomial function (F and Q are harmonic and quartic force constants, respectively)

$$V(q) = -\frac{1}{2}Fq^2 + \frac{1}{24}Qq^4 + \frac{3F^2}{2Q}$$

and the more sophisticated Manning-type⁴⁷ potential (A , D , k and r are parameters)

$$V(q) = \frac{1}{kr^2} \left[-(A + D)\operatorname{sech}^2\left(\frac{q}{2r}\right)D\operatorname{sech}^4\left(\frac{q}{2r}\right) \right]$$

were also tested. Eigenvalues and eigenfunctions were calculated numerically using a modified version of the Berkeley PES4 code⁴⁸ (see ESI† for additional information, including a list of the DFT data points, potential parameters and eigenfunctions).

Results and discussion

IRMPD spectra were measured for cluster sizes in-between $V_2O_6^-$ and $V_8O_{20}^-$ by monitoring the most abundant fragment ions. No photodissociation was observed for $V_mO_n^-$ anions smaller than $V_2O_6^-$, presumably due to the decreasing efficiency of the multiple photon absorption mechanism with decreasing cluster size. For most parent ions multiple fragmentation channels are observed, producing similar IRMPD spectra at different fragment ion masses. All observed fragmentation channels and experimental band positions are listed in Table 1. Simulated linear absorption spectra, derived from scaled harmonic frequencies and IR intensities, of the lowest energy isomers are used to aid in the assignment. The simulated spectra were generated by convoluting stick spectra, based on B3LYP/TZVP scaled harmonic frequencies and oscillator strengths (see Table 2 for the parameters of the lowest energy isomer and the ESI† for the parameters of the other isomers), with a Gaussian line shape function corresponding to a FWHM of 2.4% of the central wavelength. In principle, it would be advantageous to base an assignment on the comparison with simulated IRMPD spectra.²¹ However, such a strategy is not applicable here, because it requires detailed knowledge of the underlying potential energy surface, in particular with respect to anharmonicities and anharmonic couplings, which are generally not well characterized for transition metal oxide clusters. Discrepancies, in particular with regard to the relative band intensities and widths, which result from the different nature of the experimental and simulated spectra, are thus expected and will be discussed as we proceed. In the assignment of the spectra we thus mainly rely on the position of the allowed absorption bands and to a lesser degree on their relative intensity.

General trends

In the previous vibrational predissociation study on mono- and divanadium oxide cations three types of vibrational modes were identified in the region from 600 to 1600 cm^{-1}

Table 1 Experimental vibrational frequencies (in cm^{-1}) of $V_mO_n^-$ clusters determined from the respective IRMPD spectra, measured monitoring fragment ions mass-selectively. Vibrational frequencies are determined from band maxima or estimated based on observed shoulders (sh) formed by overlapping transitions

Parent ion	Fragment ion(s)	Position of observed bands
$V_2O_6^-$	$V_2O_5^-$	~ 975 (sh), 959, 930, 911, 888, 800, 775, 738, $\sim 620^a$
$V_2O_7^-$	$V_2O_5^-$	1112, 987, ~ 965 (sh), 952, 775, 705, 627
$V_3O_8^-$	$V_3O_7^-$	965, 922, 834, 680, 656
	$V_2O_5^-$	
	VO_3^-	
$V_4O_{10}^-$	$V_3O_8^-$	990, 670, 637, 602 ^b
$V_4O_{11}^-$	$V_4O_{10}^-$	999, 990 (sh), 976 (s), 899 (sh), 874 (sh), 824, 785 (sh), 721, 684
	$V_3O_8^-$	988, 976 (sh), 865 (s), 832 (sh), 810, 728
$V_5O_{13}^-$	$V_3O_8^-$	1000, 948, 900 (sh), 843
	$V_4O_{10}^-$	1000, 948 (sh), 906 (sh), 884 (sh), 843
	$V_5O_{12}^-$	1002, 854
$V_6O_{15}^-$	$V_3O_8^-$	962, 830
	$V_4O_{10}^-$	971, 830
	$V_5O_{13}^-$	972, 830
$V_7O_{18}^-$	$V_3O_8^-$	1004, 871
	$V_4O_{10}^-$	994, 859
	$V_5O_{13}^-$	1001, 877, 925 (sh)
	$V_6O_{15}^-$	1012, 869, 807 (sh), 739
$V_8O_{20}^-$	$V_4O_{10}^-$	1004, 871
	$V_3O_8^-$	
	$V_5O_{13}^-$	

^a Very weak. ^b Band positions shown before in ref. 22.

and assigned to (i) superoxo- ($\sim 1160 \text{ cm}^{-1}$), (ii) vanadyl- ($1060\text{--}910 \text{ cm}^{-1}$) and the (iii) V–O–V vibrational modes ($< 840 \text{ cm}^{-1}$).³⁸ A similar grouping of vibrational modes is observed for the $V_mO_n^-$ clusters: (i) superoxo- ($\sim 1100 \text{ cm}^{-1}$), (ii) vanadyl- ($1020\text{--}870 \text{ cm}^{-1}$) and the (iii) V–O–V and terminal V–O• single bond vibrational modes ($< 950 \text{ cm}^{-1}$). Based on this classification the following observations can be made (see also Fig. 1, 2, 4 and 5). (a) The only cluster that absorbs in region *i* is $V_2O_7^-$. (b) All spectra show a single, rather narrow and intense band, in some cases with additional structure, in region *ii*. (c) This band is shifted monotonically to the blue, from 959 cm^{-1} in $V_2O_6^-$ to 1004 cm^{-1} in $V_8O_{20}^-$, with the exception of the corresponding band in $V_6O_{15}^-$. (d) All clusters show absorption in region *iii*, but with some distinct differences, for example, both $V_2O_7^-$ and $V_4O_{10}^-$ show no absorption in the 800 to 925 cm^{-1} region, while all other clusters do. (e) The simplicity of the IRMPD spectrum of $V_4O_{10}^-$ is clearly different from all others, indicating a particularly interesting cluster. (f) All larger clusters, starting with $V_5O_{13}^-$, show either no or only very weak absorption below 750 cm^{-1} . (g) The V–O–V band in these spectra broadens considerably and evolves into a continuous, structureless absorption band extending from 750 to 1000 cm^{-1} in $V_8O_{20}^-$. All these observations are reproduced reasonably well by the calculations, with the exception of the last one, which we attribute to anharmonic effects (see discussion) not included in the computational model.

The closed shell anions $(V_2O_5)_nVO_3^-$, $n = 1\text{--}3$

$(V_2O_5)_nVO_3^-$ clusters are particularly stable, because they form closed-shell species, containing fully oxidized V atoms,

Table 2 Scaled harmonic vibrational frequencies (in cm^{-1}) above 550 cm^{-1} , relative intensities (in parentheses) and mode assignment for V_mO_n^- clusters from B3LYP/TZVP calculations. Scaling factors of 0.9167 (V=O modes) and 0.9832 (V–O–V modes) were taken from ref. 38. See ESI† for total energies and results of energetically higher-lying isomers

Anion	Symmetry	Type	Scaled harmonic frequency (cm^{-1})
V_2O_6^-	${}^2\text{A}' (\text{C}_s)$	V=O	945 (a' , 0.66), 937 (a' , 0.37)
		V=O/V–O–V	803 ^a /861 ^b (a' , 1.00)
V_2O_6^-	${}^2\text{B}_2 (\text{C}_{2v})$	V–O–V	784 (a' , 0.25), 733 (a'' , 0.38), 617 (a' , 0.52)
		V=O	944 (b_2 , 0.65), 937 (a_1 , 0.37)
V_2O_7^-	${}^2\text{A}'' (\text{C}_s)$	V=O/V–O–V	800 ^a /858 ^b (a_1 , 1.00)
		V–O–V	783 (a_1 , 0.24), 733 (b_1 , 0.38), 617 (a_1 , 0.52)
V_2O_7^-	${}^2\text{A}'' (\text{C}_s)$	O=O	1095 ^a (a' , 0.13)
		V=O	970 (a' , 0.57), 940 (a' , 0.67), 925 (a' , 1.00)
V_3O_8^-	${}^1\text{A}_1 (\text{C}_{2v})$	V–O–V	788 (a' , 0.89), 696 (a'' , 0.49), 632 (a' , 0.70)
		V=O	989 (a_1 , 0.18), 962 (b_1 , 0.74), 947 (b_2 , 0.37), 944 (a_1 , 0.33)
$\text{V}_4\text{O}_{10}^-$	${}^2\text{B}_2 (\text{D}_{2d})$	V–O–V	859 (a_1 , 1.00), 773 (b_1 , 0.01), 741 (a_1 , 0.00), 708 (b_2 , 0.17), 671 (b_1 , 0.49)
		V=O	995 (a_1 , 0.00), 969 ^c (e , 0.92), 968 (b_2 , 1.00)
$\text{V}_4\text{O}_{11}^-$ dioxo	${}^2\text{A}' (\text{C}_s)$	V–O–V	651 (b_1 , 0.00), 636 (a_1 , 0.00), 629 ^c (e , 0.32), 609 ^c (b_2 , 0.22), 579 (e , 0.05)
		V=O	989 (a' , 0.24), 973 (a'' , 0.88), 960 (a' , 0.87), 891 (a' , 0.15), 868 (a' , 1.00)
$\text{V}_5\text{O}_{13}^-$ pyramidal	${}^1\text{A}_1 (\text{C}_{4v})$	V–O–V	642 ^b (a' , 0.04)
		V=O	848 (a' , 0.93), 834 (a' , 0.76), 732 (a' , 0.60), 672 (a'' , 0.06), 620 (a' , 0.09), 607 (a' , 0.19), 588 (a' , 0.03)
$\text{V}_6\text{O}_{15}^-$	${}^2\text{A}' (\text{C}_s)$	V–O–V	1012 (a_1 , 0.13), 990 (a_1 , 0.21), 978 (e , 0.73), 972 (b_2 , 0.00)
		V=O	877 (a_1 , 0.49), 856 (b_2 , 0.00), 856 (e , 1.00), 667 (e , 0.07), 629 (b_1 , 0.00), 625 (b_2 , 0.00), 577 (e , 0.03), 565 (a_2 , 0.00), 564 (a_1 , 0.08)
$\text{V}_7\text{O}_{18}^-$ pyramidal	${}^1\text{A}_1 (\text{C}_{2v})$	V–O–V	1003 (a' , 0.01), 984 (a' , 0.27), 982 (a'' , 0.27), 980 (a' , 0.27), 974 (a' , 0.05), 971 (a'' , 0.05)
		V=O	915 (a' , 1.00), 900 (a'' , 0.08), 894 (a' , 0.17), 849 (a'' , 0.35), 806 (a' , 0.29), 702 (a'' , 0.08), 670 (a' , 0.04), 611 (a'' , 0.01), 601 (a' , 0.03), 589 (a' , 0.01), 583 (a'' , 0.01), 564 (a' , 0.00), 559 (a'' , 0.00)
$\text{V}_8\text{O}_{20}^-$	${}^2\text{A}' (\text{C}_s)$	V–O–V	1013 (a_1 , 0.03), 997 (a_1 , 0.13), 987 (b_2 , 0.23), 985 (b_1 , 0.29), 983 (a_1 , 0.12), 979 (a_2 , 0.00), 978 (b_1 , 0.04)
		V=O	944 (b_1 , 0.20), 937 (a_1 , 0.15), 922 (a_1 , 0.53), 894 (b_2 , 1.00), 892 (b_1 , 0.54), 890 (b_2 , 0.00), 683 (b_1 , 0.04), 645 (b_2 , 0.00), 617 (a_2 , 0.00), 604 (a_1 , 0.00), 603 (b_2 , 0.02), 599 (b_1 , 0.00), 587 (a_2 , 0.00)
$\text{V}_8\text{O}_{20}^-$	${}^2\text{A}' (\text{C}_s)$	V–O–V	1008 (a' , 0.00), 989 (a' , 0.30), 988 (a' , 0.27), 988 (a'' , 0.32), 981 (a' , 0.02), 980 (a' , 0.02), 980 (a'' , 0.01), 975 (a' , 0.01)
		V=O	952 (a' , 0.01), 943 (a'' , 0.08), 942 (a' , 0.34), 931 (a' , 0.83), 911 (a'' , 1.00), 895 (a' , 0.69), 864 (a' , 0.21), 727 (a' , 0.10), 678 (a'' , 0.03), 633 (a'' , 0.00), 619 (a'' , 0.00), 615 (a' , 0.00), 564 (a'' , 0.00), 562 (a' , 0.00)

^a Scaling factor for V=O modes applied. ^b Scaling factor for V–O–V modes applied. ^c Scaled harmonic frequency has been shown before in ref. 22.

in which all V and O atoms carry a formal valence of +V and –II, respectively. Consequently, they are characterized by high electron detachment energies and dissociation thresholds (see Table 3). The preferred dissociation channel is formation of V_3O_7^- ($n = 1$) and V_3O_8^- ($n = 2, 3$), in agreement with the calculated fragmentation energies. The IRMPD spectra of the $n = 1, 2$ and 3 member of this series, together with simulated IR spectra of the two lowest energy isomers as well as the corresponding structures are shown in Fig. 1. The three experimental IRMPD spectra show three characteristic features above 800 cm^{-1} , two strong absorption bands and a weaker feature at intermediate energies. For $n > 1$ only very weak absorption is observed below 800 cm^{-1} .

The lowest energy structure predicted for V_3O_8^- , the closed-shell ${}^1\text{A}_1$ ground state, has C_{2v} symmetry and consists of a six-ring fused with a four-ring. A D_{2d} structure that consists of four-rings, spiro-connected with a common V-atom, is found 0.46 eV higher in energy. Comparison of the experimental and simulated spectra, in particular in the 550 to 800 cm^{-1} region, favors an assignment to the C_{2v} structure, in agreement with the calculated energetics. The most intense band in the

IRMPD spectrum at 965 cm^{-1} is assigned to the four vanadyl modes. All bands observed below 900 cm^{-1} are assigned to V–O–V ring modes. The mode calculated at 859 cm^{-1} (834 cm^{-1} band) involves motion of atoms comprising the six-membered ring, while the 671 cm^{-1} mode (680 cm^{-1} band) is localized more on the four-membered ring. The other modes involve more complex deformations. The peak at 922 cm^{-1} is not reproduced in either one of the two simulated spectra and remains unassigned.

For $\text{V}_5\text{O}_{13}^-$ (center column in Fig. 1) the B3LYP calculations predict two nearly isoenergetic species, a pyramidal C_{4v} structure and a bridged C_{2v} structure only 1 meV higher in energy. A larger basis set (def2-TZVP)⁴¹ puts the C_{2v} structure 24 meV below the C_{4v} structure. CCSD(T) calculations using the B3LYP/TZVP structures, on the other hand, show a pronounced preference of 98 meV (TZVP) and 67 meV (def2-TZVP) for the pyramidal C_{4v} isomer. Better agreement between experimental and simulated spectrum is found for the pyramidal structure, consisting of two strong absorption features at 980 cm^{-1} (five V=O stretch modes) and 860 cm^{-1} (four V–O–V stretch modes) and much weaker

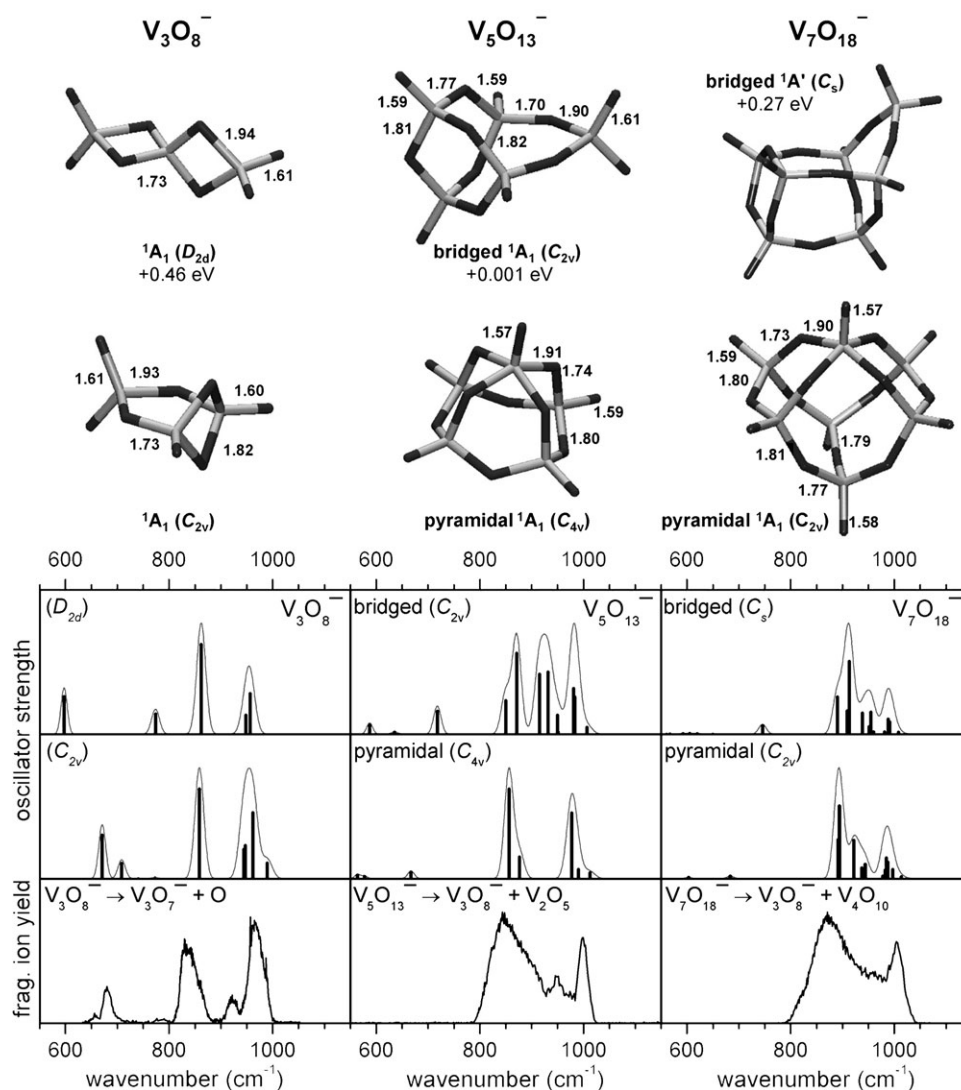


Fig. 1 Experimental IRMPD spectra (bottom) of $(V_2O_5)_{1-3}VO_3^-$ (left to right) and simulated linear IR absorption spectra, based on scaled B3LYP/TZVP frequencies and oscillator strengths of the lowest energy isomer in its electronic ground state (middle row) and an energetically low-lying isomer (top row). Optimized structures, including characteristic bonds lengths (in Å) and relative energies with respect to the ground state, are shown above the spectra. Data in part shown previously in ref. 19 and 22.

absorption below 700 cm^{-1} . In contrast, the bridged structure is characterized by three strong absorption bands in the region above 800 cm^{-1} . The additional band (930 cm^{-1}) lies in-between the 870 and 980 cm^{-1} bands that are also observed in the spectrum of the first isomer. Four rather strong transitions contribute to the absorption in the 900 – 960 region, two low-lying V=O stretch modes, involving the two vanadyl bonds on the bridging vanadium atom, and two V–O–V stretching modes, localized on the ring including the bridge. The experimental IRMPD spectra also show absorption in this region (948 cm^{-1} band), indicating that both isomers may be probed in the experiment. Best agreement between experiment and theory is achieved if both isomers are assumed to be present with a ratio of 3 : 1 in favor of the pyramidal structure.

The minimum energy structure for $V_7O_{18}^-$ (right column in Fig. 1) is a pyramidal structure (C_{2v}), but similarly to $V_5O_{13}^-$ there is a second isomer with a bridged (C_s) structure. The

energy gap between the two structures, 0.27 eV , is larger than for $V_5O_{13}^-$. The IR spectrum of the pyramidal structure is characterized by a strong absorption feature at 990 cm^{-1} (seven V=O stretch modes), a very strong one around 900 cm^{-1} (six V–O–V stretch modes) and a very weak absorption at 683 cm^{-1} . The simulated spectrum of the bridged isomer is very similar to that of the pyramidal isomer and the weak feature calculated at 746 cm^{-1} for the bridged isomer is even closer to the observed weak feature at 739 cm^{-1} in the $V_6O_{15}^-$ fragment ion channel (see Table 1).

The open shell anions $(V_2O_5)_n^-$, $n = 2$ –4

In contrast to the fully oxidized closed-shell $(V_2O_5)_nVO_3^-$ clusters, clusters of the type $(V_2O_5)_n^-$ contain an uneven number of electrons and necessarily form open-shell species. Compared to the neutral $(V_2O_5)_n$ clusters they have an extra

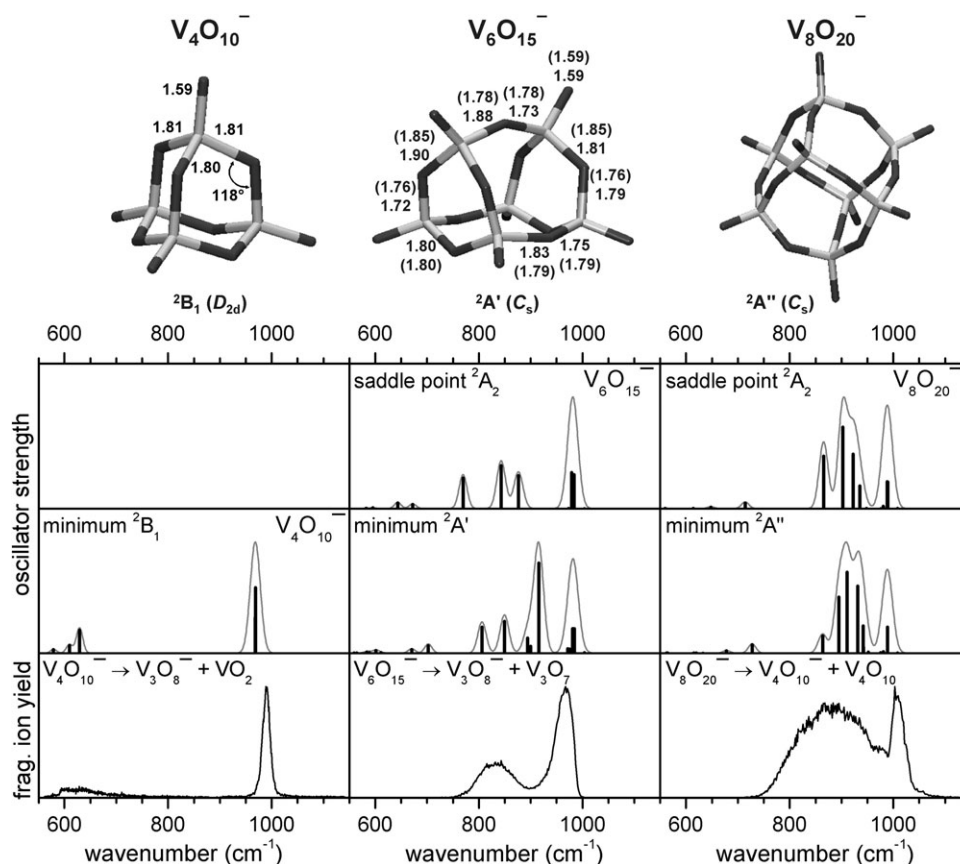


Fig. 2 Experimental IRMPD spectra (bottom) of $(V_2O_5)_{2-4}^-$ (left to right) and simulated linear IR absorption spectra, based on scaled B3LYP/TZVP frequencies and oscillator strengths of the lowest energy isomer in its electronic ground state (middle row) and an energetically low-lying first-order saddle-point (middle row) for $V_6O_{15}^-$ (left), and $V_8O_{20}^-$ (right). Optimized minimum energy structures, including characteristic bond lengths (in Å), are shown above the spectra. The 2A_2 saddle point connects two equivalent C_s structures through a C_{2v} transition state (bond lengths for the 2A_2 transition state of $V_6O_{15}^-$ are given in parentheses). Data in part shown previously in ref. 19 and 22.

electron in the unoccupied V-3d states. Consequently, the systems are characterized by somewhat lower electron detachment energies (see Table 3), but the calculated dissociation thresholds are predicted to be higher (!) than for the closed-shell $(V_2O_5)_nVO_3^-$ clusters, indicating systems of higher stability. Experimentally, predominant fragmentation leading to $V_3O_8^-$ ($n = 2-4$) and $V_4O_{10}^-$ ($n = 3, 4$) is observed.

The IRMPD spectra of the cluster series $(V_2O_5)_n^-$, $n = 2-4$ (see Fig. 2) look distinctly different from the previously discussed closed shell series, in particular for the two smaller clusters: the vanadyl band remains the strongest absorption band throughout the spectra and the position and intensity of the bands observed in the V–O–V absorption region change considerably with size. The IRMPD spectrum of $V_4O_{10}^-$ (left column in Fig. 2) looks intriguingly simple. Two features are observed in the spectrum; an intense, narrow and slightly asymmetric peak at 989 cm^{-1} and a group of weak, overlapping bands extending from 575 to 750 cm^{-1} , with a maximum at 629 cm^{-1} . The presence of only a single, rather narrow band in the spectral region of the vanadyl stretches ($>900\text{ cm}^{-1}$) and the absence of any significant absorption in-between 750 to 950 cm^{-1} suggests a highly symmetrical structure for $V_4O_{10}^-$. The spectrum of $V_6O_{15}^-$ is different in that the vanadyl band is red-shifted and the V–O–V band

intensity is relatively weak compared to the spectra of the similarly sized clusters.

For $V_4O_{10}^-$ we find a tetragonal D_{2d} structure which is minimally Jahn–Teller distorted from the T_d structure. The electronic ground state is 2B_1 . The unpaired electron is fully delocalized over all four symmetry-equivalent, four-fold-coordinated V atoms, forming one short V=O double bond (159 pm) and three V–O single bonds (180–181 pm). The four vanadyl stretches combine to one totally-symmetric mode a_1 which is IR-inactive and three IR-active e and b_2 modes which are quasi-degenerate and form the single narrow band at 969 cm^{-1} in the simulated spectrum that corresponds to the 989 cm^{-1} peak in the experimental IRMPD spectrum. The six symmetric V–O–V bond stretches also give rise to three IR active e and b_2 modes (629 and 609 cm^{-1} , respectively). They have a cumulative oscillator strength that is about 1/3 of the vanadyl bands, in satisfactory agreement with experiment. Note that the relative intensity of this bands deviates somewhat from the one published in ref. 27 due to different experimental conditions, in particular, due to the different optics used in the two experiments. The modes resulting from the six antisymmetric V–O–V bond stretches are found below 600 cm^{-1} and have vanishing intensities.

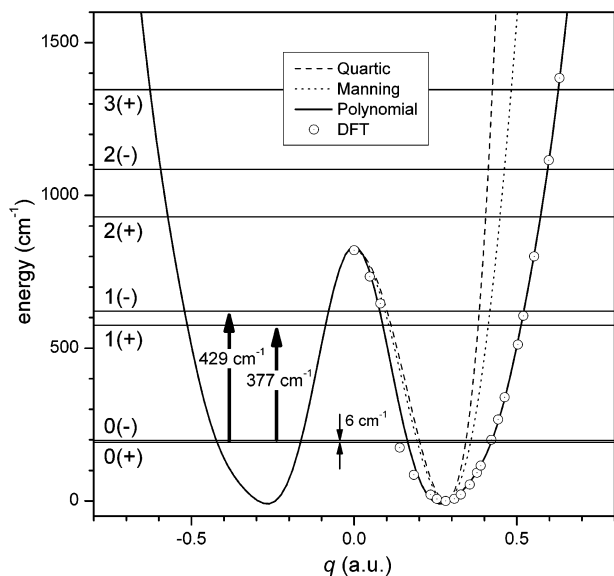


Fig. 3 Eigenvalues (horizontal lines) and transition energies of the double-well potential connecting two equivalent C_s minima *via* a C_{2v} saddle point (barrier height: 820 cm^{-1}) in $V_6O_{15}^-$. The potential energy was approximated by a 16th-degree polynomial function (solid line), which was fit to 21 points (open circles) of a relaxed DFT potential energy curve along the coordinate $q = R(O-V_1) - R(O-V_2)$. Simpler expressions for this potential using a quartic (dashed line) and a Manning-type function (dotted line), adjusted to positions of the minima and the barrier height, are also shown (see text). A qualitatively similar description is valid for $V_8O_{20}^-$ (barrier height: 730 cm^{-1}).

The lowest energy structure found for $V_6O_{15}^-$ is a distorted cage structure with C_s symmetry and a ${}^2A'$ electronic ground state (center column in Fig. 2). Other structures of higher symmetry were found $+0.10\text{ eV}$ (C_{2v} saddle point) and $+0.46\text{ eV}$ (D_{3h} saddle point of second order) higher in energy. The simulated spectrum of the C_s isomer, however, does not agree well with the experimental spectrum. In particular, the intense a' transition, calculated at 915 cm^{-1} , is not observed in the experimental spectrum. A closer look at this particular vibrational mode reveals that it is distinctly anharmonic in nature. It connects two equivalent C_s structures through the C_{2v} transition structure (2A_2 symmetry). The barrier along this coordinate is small (820 cm^{-1}). Interestingly, the simulated IR spectrum at the C_{2v} (2A_2) saddle point agrees much better with the experimental IRMPD spectrum of $V_6O_{15}^-$ (Fig. 2), due to the absence of the intense 915 cm^{-1} band. In order to determine the transition energies of the double-well potential, we solved the vibrational eigenvalue problem for this vibrational mode using the relaxed DFT potential energy along the corresponding normal coordinate (see Fig. 3 and Table 4). The first four vibrational energy levels lie below the barrier. The tunneling splittings between $0(\pm)$ and $1(\pm)$ are 6 and 46 cm^{-1} , respectively. The $1(-) \leftarrow 0(+)$ and $1(+) \leftarrow 0(-)$ transition energies ($377, 429\text{ cm}^{-1}$) are less than half and their intensities significantly smaller than the harmonic values. The simpler quartic and Manning-type expressions for the double-well potential also predict a red-shifted transition, but yield too large transition energies, due to a too steep increase of the potential with increasing q (see Fig. 3 and Table 4). Summar-

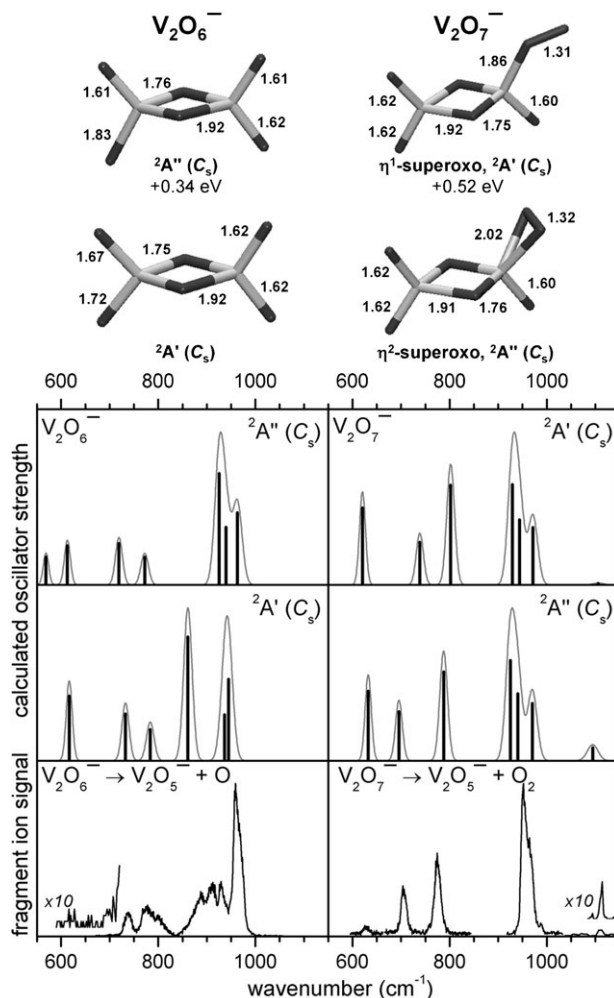


Fig. 4 Experimental IRMPD spectra (bottom) of $V_2O_6^-$ and $V_2O_7^-$ and simulated linear IR absorption spectra, based on scaled B3LYP/TZVP frequencies and oscillator strengths of the lowest energy isomer in its electronic ground state (middle row) and an energetically low-lying isomer (top row). Optimized structures, including characteristic bonds lengths (in Å) and relative energies with respect to the ground state, are shown above the spectra. Data in part shown previously in ref. 19 and 22.

izing, the simulations confirm that neither the fundamental nor any other excitations of this vibration directly contribute to the IR spectrum of $V_6O_{15}^-$ in the discussed region.

The lowest energy structure found for $V_8O_{20}^-$ is a distorted six-face cube structure (see right column in Fig. 2). Localization of the unpaired electron in the ${}^2A'$ ground state leads to symmetry lowering from O_h to C_s . Of the eight vanadyl modes three contribute significantly to the vanadyl band at 988 cm^{-1} , found at 1004 cm^{-1} in the experimental IRMPD spectrum. The V–O–V bonds, which correspond to the edges of the $V_8O_{20}^-$ cube, combine to form the broad feature predicted at 911 cm^{-1} . Five V–O–V modes contribute in the $850\text{--}950\text{ cm}^{-1}$ region, producing a broader feature, centered at 856 cm^{-1} , with a width of $\sim 60\text{ cm}^{-1}$. The assignment of the 871 cm^{-1} band in the experimental IRMPD spectrum to V–O–V modes is straightforward. Note that, similar to $V_6O_{15}^-$ there also exist two equivalent C_s structures for $V_8O_{20}^-$, which are

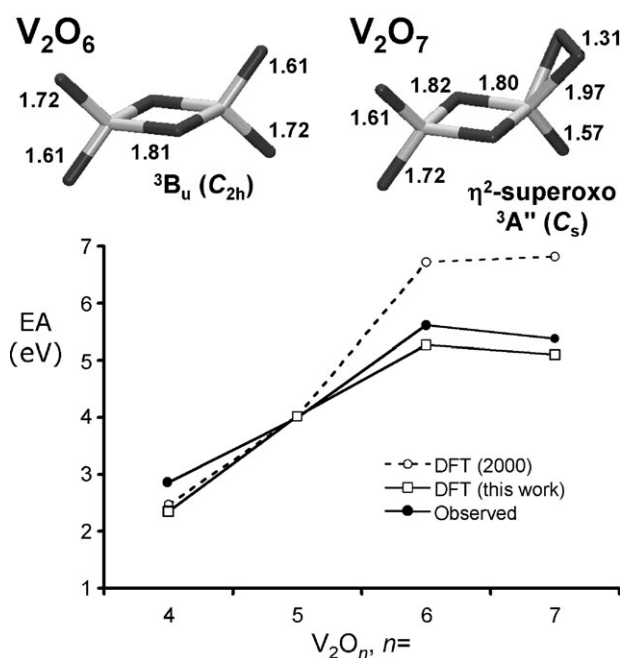


Fig. 5 Electronic ground state structures of the neutral V_2O_6 and V_2O_7 clusters (top, bond lengths in Å) and electron affinities (EA, in eV) for V_2O_n clusters as function of oxygen content n (bottom). Observed values taken from ref. 15, compared to DFT results from ref. 16, DFT(2000), and the present study.

separated by a shallow barrier (730 cm^{-1}). A significant redshift of this transition, below the measurement window, is also predicted for $V_8O_{20}^-$ (see Table 4). However, the relative intensity of this mode (864 cm^{-1}) is predicted to be considerably smaller and therefore the effect of the double-well potential on the simulated IR spectrum is not as marked as for $V_6O_{15}^-$, as evidenced by similar IR spectra predicted for the C_s minima and C_{2v} saddle point (see Fig. 2). The anharmonic nature of this mode may contribute in a different way to the IR spectrum of $V_8O_{20}^-$ (and also of $V_6O_{15}^-$). Anharmonic coupling and hot band excitation may be the source of the observed broadening of the V–O–V band, which appears roughly twice as wide in the measured spectrum compared to the simulated spectra. Interestingly, the width of this band is nearly identical to the width of the corresponding band observed in the electron energy loss spectrum of a V_2O_5

Table 3 Fragmentation energies and vertical detachment energies (VDE) in eV. Italic numbers correspond to observed fragmentation channels

Parent ion	Fragment								VDE
	O	O ₂	VO ₂	VO ₃	VO ₃ ⁻	V ₂ O ₅	V ₃ O ₈	V ₄ O ₁₀	
$V_2O_6^-$	3.93	4.75		5.26	5.26				5.70
$V_2O_7^-$	3.05	1.79							5.55
$V_3O_8^-$	5.53		6.32	6.40	6.35	6.35			6.08
$V_4O_{10}^-$	6.04		5.74			6.92			4.49
$V_4O_{11}^-$	2.05	2.90		3.95		5.04			6.66
$V_5O_{13}^-$			6.91	4.90	5.24	5.42			—
$V_6O_{15}^-$			5.16			4.84			5.28
$V_7O_{18}^-$				4.99		4.92	5.01	3.81	—
$V_8O_{20}^-$						4.87		3.18	5.48

Table 4 Eigenvalues and transition energies (in cm^{-1}) for the anharmonic vibrational mode connection of the two equivalent C_s minima using the quartic and Manning potentials in $V_6O_{15}^-$ and $V_8O_{20}^-$. For $V_6O_{15}^-$, results of the polynomial fit to the relaxed DFT potential energy curve are also listed. Estimated transition intensities normalized to the intensity of the harmonic fundamental transition are given in parentheses (see page 5 in ESI† for details)

State/ transition	$V_6O_{15}^-$			$V_8O_{20}^-$	
	Quartic	Manning	Polynomial fit	Quartic	Manning
0(+)	342	294	192	271	235
0(-)	353	303	198	275	238
1(+)	838	767	575	684	627
1(-)	1023	892	621	785	694
2(+)	1395	1218	930	1063	952
2(-)	1791	1517	1085	1340	1162
3(+)	2240	1861	1346	1663	1421
0(+) \rightarrow 0(-)	11	9	6 (1.3)	4	3
0(+) \rightarrow 1(-)	681	598	429 (0.11)	514	459
0(+) \rightarrow 2(-)	1449	1223	893 (2.4×10^{-4})	1069	928
0(-) \rightarrow 1(+)	485	464	377 (0.11) ^a	408	389
0(-) \rightarrow 2(+)	1042	916	732 (1.1×10^{-4}) ^a	788	714
0(-) \rightarrow 3(+)	1887	1558	1148 (2.3×10^{-5}) ^a	1388	1183

^a Scaled by 0.65, the Boltzmann distribution factor for an ion vibrational temperature of 20 K.

surface,⁴⁹ which also probes vibrational states, indicating that the pronounced broadening is not an artifact of the IRMPD mechanism.²²

As previously reported,²⁴ the transition from delocalized to localized electrons upon going from $V_4O_{10}^-$ to $V_6O_{15}^-$ in the series of $(V_2O_5)_n^-$ clusters is only correctly described when a hybrid functional with the right admixture of Fock exchange such as B3LYP is applied. In contrast, BLYP (no Fock exchange) yields delocalization (and fully symmetric structures) for all three systems, whereas BHLYP (50% Fock exchange) enforces localization even for $V_4O_{10}^-$. Additional evidence for this size-dependent symmetry lowering is provided by recent anion photoelectron spectra.⁵⁰ Reorganization energies obtained as differences of vertical and adiabatic electron detachment energies have been determined and both observed and calculated values are found to be substantially larger for $V_6O_{15}^-$ and $V_8O_{20}^-$ than for $V_4O_{10}^-$. For further support, single point CCSD(T) calculations have been made (at the BHLYP equilibrium structures) for $V_4O_{10}^-$ and $V_6O_{15}^-$. Table 5 shows the results. They confirm for $V_4O_{10}^-$ that the D_{2d} structure has a lower energy than the C_s isomer, whereas for $V_6O_{15}^-$ the C_{2v} structure has a higher energy than the C_s isomer. That an increasing admixture of Fock exchange (connected with increasing self-interaction correction) leads to an increasing tendency for electron localization has been found before,⁵¹ but B3LYP is not always the right solution. For the case of electron holes in silica, BHLYP is needed to get the correct localization of the hole on one oxygen site.⁵² On the contrary, in vanadium oxide cages with methoxo ligands, $V_4O_9(OCH_3)^-$ and $V_4O_8(OCH_3)_2^-$, B3LYP incorrectly localizes the extra electrons at the vanadium sites with the methoxo ligands.²⁷

The oxygen-rich clusters $V_2O_6^-$, $V_2O_7^-$, and $V_4O_{11}^-$

The clusters $V_2O_6^-$, $V_2O_7^-$, and $V_4O_{11}^-$ all contain more oxygen atoms than are formally required to fully oxidize all

Table 5 Relative stability of minima (Min) and saddle points (SP) (kJ mol⁻¹) predicted by B3LYP in comparison to CCSD(T)/TZVP single point calculations^a

System	Isomer	State	B3-LYP		RCCSD(T)	UCCSD(T)
V ₂ O ₆ ⁻	O ₂ VO ₂ VO ₂	C _s ⁻² A'	0.0	Min	7.9	4.0 [2.6] ^b
		C _{2v} ⁻² B ₂	0.0	SP	0.0	0.0
		D _{2h} ⁻² B _{1u}	21.6	SP	28.7	27.1
		C _s ⁻² A''	32.9	Min		
		D _{2h} ⁻² B _{3g}	39.3	SP		
V ₂ O ₇ ⁻	η ² -Superoxo η ¹ -Superoxo η ¹ -Superoxo	C _s ⁻² A''	0.0	Min		
		C _s ⁻² A''	32.1	SP		
		C _s ⁻² A'	50.3	Min		
		C _s ⁻² A'	0.0 (0.0) ^c	Min	0	0
V ₄ O ₁₁ ⁻	Dioxo-bridged Dioxo-open μ-(η ² :η ²)-Peroxoanion μ-(η ² :η ²)-Peroxo μ-(η ² :η ²)-Peroxo η ² -Peroxo	C _s ⁻² A'	2.4 (2.4) ^c	Min	19.4	17.0
		C _{2v} ⁻² B ₂	15.0 (13.0) ^c	Min	11.3	11.0
		C _s ⁻² A'	21.4	Min	16.7	18.0
		C _{2v} ⁻² A ₁	31.4	SP	13.7	12.6
		C _s ⁻² A'	35.1	Min	56.2	57.3
		D _{2d}	0.0	Min	0.0 ^a	
V ₅ O ₁₃ ⁻	Pyramidal Bridged	C _s	6.9	SP	33.3 ^a	
		C _{4v}	0.0	Min	0.0	
V ₆ O ₁₅ ⁻		C _{2v}	0.1 (-2.3) ^c	Min	9.4 (6.7) ^c	
		C _s	0.0	Min	0.0 ^a	
		C _{2v}	9.4 (10.5) ^c	SP	9.0 ^a	

^a Calculated at the B3LYP equilibrium structure for V₄O₁₀⁻, V₆O₁₅⁻ and V₈O₂₀⁻, see ref. 24; in all other cases at the B3LYP equilibrium structure. ^b Structures optimized by UCCSD(T) using a ROHF reference function (ACES code).⁴⁵ ^c Calculations using the larger def2-TZVP basis set [6s4p4d1f]/[5s3p2d1f].⁴¹

V-atoms and thus may form characteristic oxo groups. It is interesting to see how this influences the structure and energetics of these species. Peroxo (and also superoxo) groups are of interest because they play a role in the reoxidation of vanadium oxide species in catalytic processes,²⁶ e.g., peroxo groups may be formed in the reoxidation of vanadium III to vanadium V sites, V^{III}(O-)₃ + O₂ → (O₂)V^V(O-)₃. Superoxo groups form one bond with the metal site, while peroxo groups form two. In an ionic picture they correspond to (O₂)⁻ and (O₂)²⁻ species, respectively, with the additional electrons in antibonding p-p orbitals. Therefore, the O-O bond distance increases in the series (gas phase) O₂, (O₂)⁻, and (O₂)²⁻ and the vibrational frequencies decrease. Superoxo and peroxo groups are expected to be present in gas phase species in which the oxygen content is larger than that given by the highest oxidation state for vanadium, VO_{2.5}, VO₂⁺ or VO₃⁻. An example is V₂O₆⁺, for which we have identified a superoxo vibration at 1160 cm⁻¹.³⁸

The oxygen-rich species V₂O₆⁻, V₂O₇⁻, and V₄O₁₁⁻ studied here are characterized by considerably lower dissociation thresholds and relatively high vertical detachment energies (see Table 3) and the predicted dissociation channels leading to loss of either an O atom (V₂O₆⁻ and V₄O₁₁⁻) or an O₂ molecule (V₂O₇⁻) agree with the experimentally observed fragmentation. Loss of molecular oxygen rather than two oxygen atoms is suggested, because photodissociation of V₂O₇⁻ also with a strongly attenuated FELIX beam yields exclusively V₂O₅⁻. The IRMPD spectra of these species are different from those of the other clusters in that they show pronounced absorption in the 700–800 cm⁻¹ region in addition to the strong vanadyl stretching band in-between 950 and 1000 cm⁻¹.

The lowest energy structure found for V₂O₆⁻ by B3LYP has C_s symmetry and consists of a four-membered V-O-V-O ring

plus two singly-coordinated oxygen atoms on each V atom (see Fig. 4). There is, however, a C_{2v} transition structure at only slightly higher energy (0.1 meV). The C_s structure is an artificial broken symmetry structure and the C_{2v} structure is the likely global minimum energy structure. This is supported by coupled cluster calculations (see Table 5). Localization of the unpaired electron on one of the (O=)₂V(O-)₂ parts leads to a pronounced asymmetry in the lengths of the terminal V-O bonds (1.62 and 1.69 Å) as well as the ring V-O bonds (1.92 and 1.75 Å). This confirms the findings in ref. 53, whereas an earlier DFT study¹⁶ reported only the D_{2h}⁻²B_{1u} structure of V₂O₆⁻, which is a saddle point. The spectra obtained by B3LYP for the C_s and C_{2v} structures are, however, virtually identical. Moreover, the simulated vibrational spectrum of the ²A' (C_s) structure of V₂O₆⁻ shows some similar features with the experimental IRMPD spectrum, but overall agreement is poor, even though it is better than for the next lowest electronic state of ²A'' symmetry. An assignment in this case is not possible. The discrepancies between the calculated and experimental spectra are presumably introduced by the combination of a relatively high dissociation threshold (see Table 3) with a modest density of states in V₂O₆⁻, the smallest cluster studied here, leading to an enhancement of the multiphoton character of the IRMPD spectrum.

The lowest energy isomer found for V₂O₇⁻ (see Fig. 4) has a V₂O₆⁻-like structure of C_s symmetry, in which a terminal oxygen atom is replaced by a superoxo-unit, see also ref. 16. Good agreement between experimental and simulated peak positions is found, supporting the assignment to one superoxo mode, calculated at 1095 cm⁻¹, three modes involving different combinations of the symmetric stretching motion along the three vanadyl bonds (970, 940 and 925 cm⁻¹) and the three characteristic V-O-V-O ring modes (788, 696 and 632 cm⁻¹).

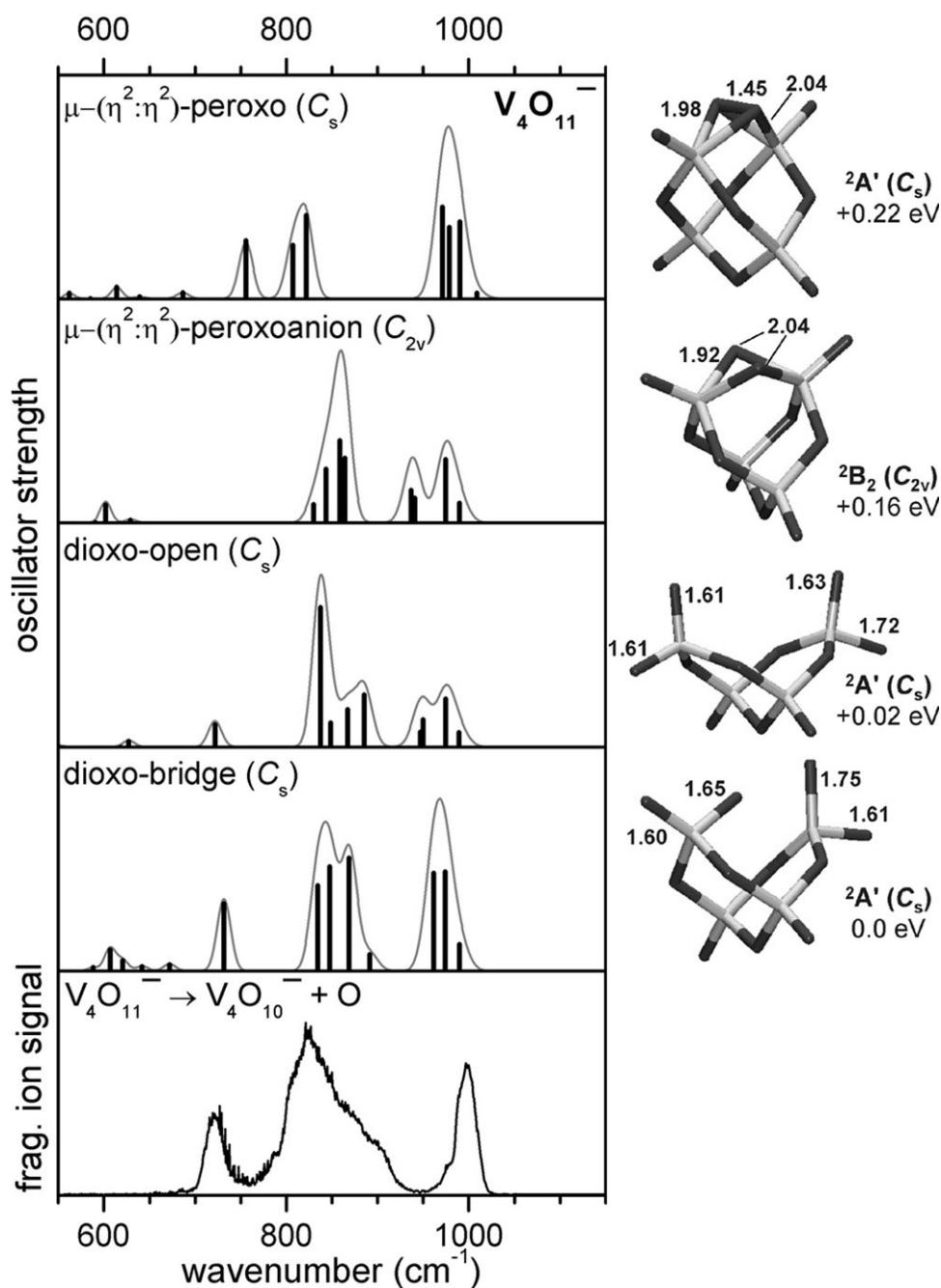


Fig. 6 Experimental IRMPD spectrum (bottom) of $V_4O_{11}^-$ and simulated linear IR absorption spectra, based on scaled B3LYP/TZVP frequencies and oscillator strengths of four low energy isomers for $V_4O_{11}^-$. Optimized structures, including characteristic bonds lengths (in Å) and relative energies with respect to the ground state, are shown to the right of the spectra. Data in part shown previously in ref. 22.

A comparison of the electron affinities (EA) of $V_2O_n^-$ clusters ($n = 4-7$) (see Fig. 5) derived from anion photoelectron spectra¹⁵ and DFT calculations provides an additional check, if the most stable isomers have been found in the DFT calculations. For $n = 6, 7$ unusually large deviations of more than 1 eV have been reported for the previous calculations¹⁶ and the observed decrease in EA from $n = 6$ to $n = 7$ was not reproduced by the calculations. This was an indication that the previous DFT calculations¹⁶ may not have considered the right geometric structures or electronic ground states. Whereas the

η^2 -superoxo $V_2O_7^-$ structure (C_s - ${}^2A''$) of ref. 16 is confirmed by the present study, the D_{2h} - ${}^2B_{1u}$ structure of $V_2O_6^-$ is not. However, with the present, more stable C_s - ${}^2A'$ (or C_{2v} - 2B_2) $V_2O_6^-$ structures the calculated EA and its deviation from the measured EA would be even larger. The reason is found in the energy of the neutral species (Fig. 5). While the structure types of ref. 16 were right, the electronic states were not. Both V_2O_6 and V_2O_7 have triplet ground states that are 1.67 and 1.71 eV, respectively, below the closed shell singlet states reported in ref. 16. With the correct ground states of the neutrals the calculated

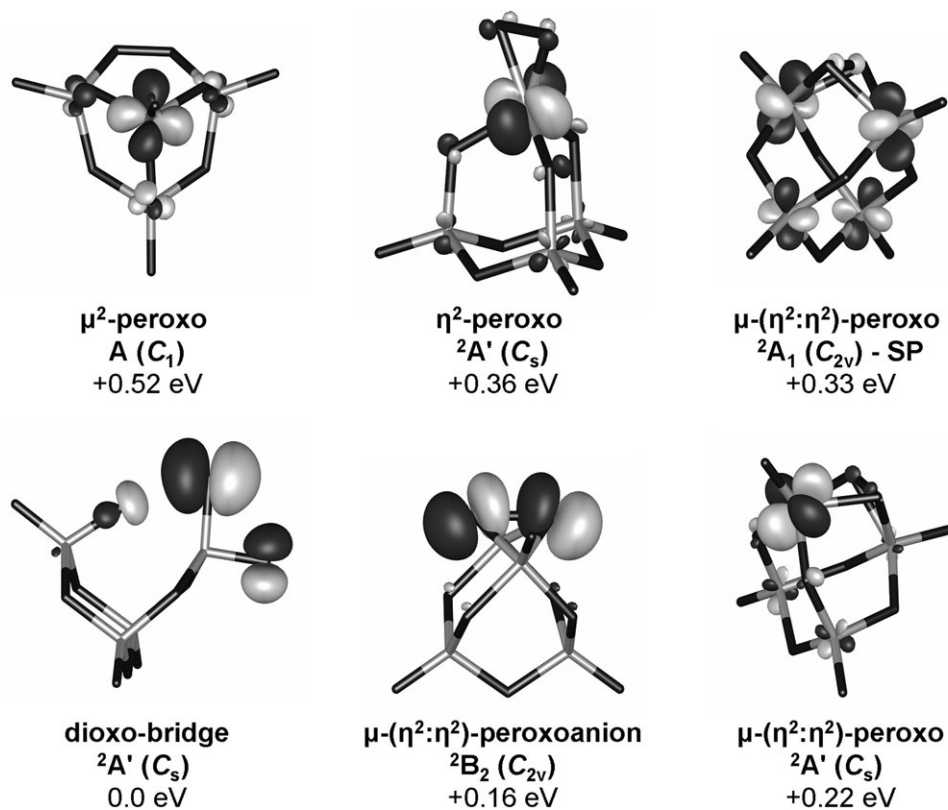


Fig. 7 Singly occupied molecular orbitals of six $V_4O_{11}^-$ isomers and relative energies with respect to the electronic ground state (see text).

EA (5.27 and 5.10 eV, respectively) agree with the observed ones within the typical few tenths of eV and, in particular, show the right decrease from $V_2O_6^-$ to $V_2O_7^-$.

For $V_4O_{11}^-$ the best agreement between the experimental and simulated IR spectra is not found for the caged structure $\mu-(\eta^2:\eta^2)$ -peroxo (top spectrum in Fig. 6), derived from the exceptionally stable V_4O_{10} (see below), but a very different, open structure termed “DIOXO-bridge” (2nd spectrum from the bottom in Fig. 6). This isomer is formally obtained by replacing O in one of the V–O–V bridges by μ^2 -O–O (peroxo) and by subsequently opening the V–O–O–V bridge. As a result, we have a stretched (1.65 Å) vanadyl group on one of the V sites, with the oxygen still in a “bridging” position, and a terminal V–O• group with the unpaired electron on the other V site (1.75 Å). The former leads to an unusually red-shifted and intense V=O mode at 868 cm^{-1} , directly next to the strong V–O–V modes at 848 , 834 and 732 cm^{-1} . The original vanadyl groups on these V sites are slightly longer (1.60 and 1.61 pm) than in $V_4O_{10}^-$ and have vibrations at 960 and 891 cm^{-1} , respectively; the other vanadyl groups are calculated at 989 and 973 cm^{-1} . There is another dioxo-isomer, “DIOXO-open”, with a more open structure and the long V–O• bond pointing away from the second dioxo site. Its calculated IR spectrum is similar to that of the “DIOXO-bridge”, *i.e.*, this isomeric form may contribute to the experimental IR spectrum. B3LYP/TZVP predicts that the DIOXO-open isomer is only 0.02 eV higher than the DIOXO-bridge, but CCSD(T) single point calculations increase this difference to 0.20 eV (Table 5).

Thus, $V_4O_{11}^-$ is a particularly interesting case, because it does not exhibit a peroxo group, as one would expect based on the structure of the corresponding neutral species. Formally, the neutral V_4O_{11} cluster is obtained when replacing a O^{2-} by an $(O_2)^{2-}$ ion in the V_4O_{10} cage. When the replacement is made in a V–O–V bridge, we get either a $\mu-(\eta^2:\eta^2)$ -peroxo or a μ^2 -peroxo group. The latter is 0.05 eV less stable. We can also replace a vanadyl oxygen and obtain the η^2 -peroxo group described before,¹⁶ which, however, is 0.23 eV less stable. (DFT studies have also been made for $\mu-(\eta^2:\eta^2)$ - and η^2 -peroxo groups on the V_2O_5 (001) surface.⁵⁴) What happens if an electron is added to the different V_4O_{11} peroxo isomers? In V_4O_{10} , as in all vanadium oxides with vanadium in the +V oxidation state, the lowest unoccupied states are vanadium 3d-states. In peroxo compounds, antibonding O (2p–2p) σ^* states are also available among the low-lying unoccupied states (see Fig. 7). If we add an electron to the V d-states of the $\mu-(\eta^2:\eta^2)$ -peroxo isomer, it either distributes among the four V sites resulting in a symmetric C_{2v} structure (Fig. 7, top right) or it localizes at one of the neighboring V sites resulting in a C_s structure with different bond distances from the two neighboring V sites to the peroxo unit (Fig. 7, bottom right, top spectrum in Fig. 6). On the B3LYP/TZVP potential energy surface, the former (C_{2v}) structure is a saddle point and only the latter (C_s) is a minimum. However, CCSD(T) single point calculations indicate that this symmetry breaking may be an artifact of B3LYP. The η^2 - and μ^2 -isomers of $V_4O_{11}^-$ have even higher energies than the $\mu-(\eta^2:\eta^2)$ peroxo isomer. Upon adding an electron to the η^2 - and the μ^2 -isomers of V_4O_{11} , the

extra electron occupies d-states at the V-site connected to the peroxy unit in the η^2 -isomer (Fig. 7, top center), whereas in the μ^2 -peroxy isomer it is on one of the V sites “opposite” to the peroxy unit (Fig. 7, top left).

However, we obtain lower energy $V_4O_{11}^-$ isomers if we add the electron to the antibonding (2p–2p) σ^* orbital of the O_2 unit. In the case of the μ -(η^2 : η^2)-peroxy isomer, formally a $(O_2)^{3-}$ species, “peroxoanion”, is created with a bond order of 0.5 compared to 1.0 in $(O_2)^{2-}$. This explains the long O–O bond of 2.04 Å in this μ -(η^2 : η^2) “peroxoanion” isomer with C_{2v} structure (Fig. 7, bottom center; Fig. 6, second spectrum from top). CCSD(T) calculations show that this is the second most stable isomer of $V_4O_{11}^-$. In the case of the μ^2 -peroxy isomer, adding an electron to the antibonding (2p–2p) σ^* orbital of the O–O-unit, opens the V–O–O–V bridge completely and the lowest energy dioxy structure shown in Fig. 6 is obtained. In summary, conversion of the neutral cluster into a cluster anion induces a qualitative change in the structure and the peroxy group is no longer a structural feature of the most stable $V_4O_{11}^-$ isomers. As CCSD(T) calculations indicate, the second and third most stable isomers feature a O_2 unit in μ -(η^2 : η^2) configuration, with the additional electron either in the O_2 unit (μ -(η^2 : η^2) “peroxoanion”, $C_{2v-2}B_2$) or in vanadium d-states (μ -(η^2 : η^2) peroxy, $C_{2v-2}A_1$).

The existence of the two lowest energy isomers of $V_4O_{11}^-$, dioxy-bridge and μ -(η^2 : η^2) “peroxoanion” finds a simple explanation in adding the extra electron to antibonding orbitals of the peroxy group of the neutral parent compound, V_4O_{11} . However, our structure search was originally limited to the different peroxy structures we knew from the neutral V_4O_{11} cluster. Only the insufficient agreement of the observed IR spectrum with the one predicted for the lowest peroxy structure, the μ -(η^2 : η^2) peroxy isomer (Fig. 6), was the motivation to apply a global optimization scheme. This scheme has generated the two lowest energy structures for $V_4O_{11}^-$. Even with the genetic algorithm, there is no guarantee that the global minimum structure is found. It is therefore important that the IRMPD spectrum has been measured which is in sufficient agreement with the B3LYP prediction for the “dioxy” structure, thus confirming that the latter is indeed likely to be the global minimum structure.

Conclusions

Our results show that experimental IRMPD spectra in combination with scaled harmonic B3LYP vibrational frequencies can be used to identify three characteristic absorption regions of vanadium oxide anions, namely the oxo, vanadyl, and V–O single bond region. With the exception of $V_2O_6^-$, the agreement between simulated linear IR absorption spectra and experimental multiple photon IR photodissociation spectra is often sufficient to identify a single electronic and structural isomer responsible for the main absorption features. In several cases ($V_4O_{11}^-$, $V_5O_{13}^-$, and $V_7O_{18}^-$) additional isomers may be present, leading to additional, weaker absorption features.

A structural transition is observed with cluster size. While di- and trivanadium oxide anions are characterized by open structures involving 4-membered V–O–V–O rings, this motif is replaced by the less strained, more stable 6- and 8-membered

rings in the larger clusters. $V_4O_{10}^-$ is the first cage structure. The most stable structural motif in larger clusters is a 4-fold coordinated V-atom, which forms three V–O–V single bonds and a single terminal double bond. 5-Fold coordinated V-atoms and 4-fold coordinated ones bound to two terminal O-atoms are also found and lead to isomers of similar energy.

Genetic algorithms prove vital to finding the global minimum in some cases. To come up with structural candidates for larger metal oxide clusters chemical intuition may not be sufficient. The wealth of structural and electronic isomers can lead to unusual structures and algorithms that probe a larger part of the potential energy landscape become important.

In the open shell $(V_2O_5)_n^-$ anions two competitive effects are observed, *i.e.*, electron delocalization *vs.* stabilization through symmetry lowering. In order to minimize electron–electron repulsion, structures are favored in which the additional electron is delocalized over d orbitals of the V atoms. However, this requires favorable atomic orbital overlap, which is only present in the $n = 2$ anion. In the $n = 3, 4$ anions this overlap is less favorable and the electron is consequently localized at a single V-atom, leading to a distortion of the cage structure and symmetry lowering. The localization/delocalization behavior of the extra electron is only correctly predicted by B3LYP, while BHLYP and BLYP fail. The difficulty of the latter two functionals has important consequences in reliably describing electron localization on surfaces and needs to be recognized.

As a result of this symmetry lowering in the larger cluster anions there exist many symmetry equivalent local energy minima. The barriers to interconversion between these can be small and the vibrational normal modes connecting these minima can be markedly anharmonic, leading to a breakdown of the harmonic approximation and a characteristic signature in the IR spectrum of these species. These effects are not restricted to the gas phase, but are also important in explaining the IR spectrum of a V_2O_5 surface. On the other hand, the similarities and differences of the IR-spectra of $V_8O_{20}^-$ and that of a solid surface²² make $V_8O_{20}^-$ an interesting candidate for studying surface absorption and reactivity on a model system in the gas phase.

Acknowledgements

This work has been supported by the Collaborative Research Center 546 of the Deutsche Forschungsgemeinschaft. The authors thank G. von Helden, A. Fielicke and K. Rademann (Berlin) for their support, D. Neumark (Berkeley) for supplying a copy of the PES4 program, P. Ugliengo (Torino) for helpful discussions on solutions for the double-well potential in general and the Manning potential in particular. We also gratefully acknowledge the support of the Stichting voor Fundamenteel Onderzoek der Materie (FOM) in providing the required beam time on FELIX and highly appreciate the skilful assistance of the FELIX staff.

References

1. B. M. Weckhuysen and D. E. Keller, *Catal. Today*, 2003, **78**, 25–46.
2. M. S. Whittingham, *Chem. Rev.*, 2004, **104**, 4271–4301.

3. L. A. L. de Almeida, G. S. Deep, A. M. N. Lima, I. A. Khrebtov, V. G. Malyarov and H. Neff, *Appl. Phys. Lett.*, 2004, **85**, 3605–3607.
4. L. Krusin-Elbaum, D. M. Newns, H. Zeng, V. Derycke, J. Z. Sun and R. Sandstrom, *Nature*, 2004, **431**, 672–676.
5. N. Magg, B. Immaraporn, J. B. Giorgi, T. Schroeder, M. Bäumer, J. Döbler, Z. L. Wu, E. Kondratenko, M. Cherian, M. Baerns, P. C. Stair, J. Sauer and H.-J. Freund, *J. Catal.*, 2004, **226**, 88–100.
6. U. Heiz and E. L. Bullock, *J. Mater. Chem.*, 2004, **14**, 564–577.
7. D. K. Böhme and H. Schwarz, *Angew. Chem., Int. Ed.*, 2005, **44**, 2336–2354.
8. E. B. Rudnyi, E. A. Kaibicheva and L. N. Sidorov, *J. Chem. Thermodyn.*, 1993, **25**, 929–947.
9. R. C. Bell and K. A. Zemski, D. R. Justes and A. W. Castleman Jr., *J. Chem. Phys.*, 2001, **114**, 798–811.
10. A. Dinca, T. P. Davis, K. J. Fisher, D. R. Smith and G. D. Willett, *Int. J. Mass Spectrom. Ion. Proc.*, 1999, **182/183**, 73–84.
11. R. C. Bell and A. W. Castleman, Jr, *J. Phys. Chem. A*, 2002, **106**, 9893–9899.
12. T. Waters, G. N. Khairallah, S. Wimala, Y. C. Ang, R. A. J. O'Hair and A. G. Wedd, *Chem. Commun.*, 2006, 4503–4505; T. Waters, A. G. Wedd and R. A. J. O'Hair, *Chem.–Eur. J.*, 2007, **13**, 8818–8829.
13. F. Dong, S. Heinbuch, Y. Xie, J. J. Rocca, E. R. Bernstein, Z. C. Wang, K. Deng and S. G. He, *J. Am. Chem. Soc.*, 2008, **130**, 1932–1943.
14. H. Wu and L.-S. Wang, *J. Chem. Phys.*, 1998, **108**, 5310–5318.
15. H. J. Zhai and L.-S. Wang, *J. Chem. Phys.*, 2002, **117**, 7882–7888.
16. S. F. Vyboishchikov and J. Sauer, *J. Phys. Chem. A*, 2000, **104**, 10913–10922.
17. M. Maier-Borst, D. B. Cameron, M. Rokni and J. H. Parks, *Phys. Rev. A*, 1999, **59**, R3162–R3165.
18. A. Lechtken, D. Schooss, J. R. Stairs, M. N. Blom, F. Furche, N. Morgner, O. Kostko, B. von Issendorff and M. M. Kappes, *Angew. Chem., Int. Ed.*, 2007, **46**, 2944–2948.
19. K. R. Asmis, A. Fielicke, G. von Helden and G. Meijer, in *The Chemical Physics of Solid Surfaces, Atomic Clusters: From Gas Phase to Deposited*, ed. D. P. Woodruff, Elsevier, Amsterdam, 2007, vol. 12, pp. 327–375.
20. M. A. Duncan, *Int. J. Mass Spectrom.*, 2000, **200**, 545–569.
21. J. Oomens, B. G. Sartakov, G. Meijer and G. von Helden, *Int. J. Mass Spectrom.*, 2006, **254**, 1–19.
22. K. R. Asmis and J. Sauer, *Mass Spectrom. Rev.*, 2007, **26**, 542–562; K. R. Asmis and J. Sauer, *Mass Spectrom. Rev.*, 2008, **27**, 205.
23. G. von Helden, I. Holleman, G. M. H. Knippels, A. F. G. van der Meer and G. Meijer, *Phys. Rev. Lett.*, 1997, **79**, 5234–5237.
24. K. R. Asmis, G. Santambrogio, M. Brümmer and J. Sauer, *Angew. Chem., Int. Ed.*, 2005, **44**, 3122–3125.
25. S. F. Vyboishchikov and J. Sauer, *J. Phys. Chem. A*, 2001, **105**, 8588–8598.
26. S. Guimond, M. Abu Haija, S. Kaya, J. Lu, J. Weissenrieder, S. Shaikhutdinov, H. Kühlenbeck, H. J. Freund, J. Döbler and J. Sauer, *Top. Catal.*, 2006, **38**, 117–125; M. Abu Haija, S. Guimond, Y. Romanyshyn, A. Uhl, H. Kühlenbeck, T. K. Todorova, M. V. Ganduglia-Pirovano, J. Döbler, J. Sauer and H. J. Freund, *Surf. Sci.*, 2006, **600**, 1497–1503.
27. S. Feyel, H. Schwarz, D. Schröder, C. Daniel, H. Hartl, J. Döbler, J. Sauer, G. Santambrogio, L. Wöste and K. R. Asmis, *ChemPhysChem*, 2007, **8**, 1640–1647.
28. K. R. Asmis, M. Brümmer, C. Kaposta, G. Santambrogio, G. von Helden, G. Meijer, K. Rademann and L. Wöste, *Phys. Chem. Chem. Phys.*, 2002, **4**, 1101–1104.
29. D. Oepf, A. F. G. van der Meer and P. W. van Amersfoort, *Infrared Phys. Technol.*, 1995, **36**, 297–308.
30. J. Oomens, A. G. G. M. Tielens, B. Sartakov, G. von Helden and G. Meijer, *Astrophys. J.*, 2003, **591**, 968–985.
31. M. Nee, C. Kaposta, A. Osterwalder, C. Cibrian Uhalte, T. Xie, A. Kaledin, S. Carter, J. M. Bowman, G. Meijer, D. M. Neumark and K. R. Asmis, *J. Chem. Phys.*, 2004, **121**, 7259–7268.
32. R. Ahlrichs, M. Bär, M. Häser, H. Horn and C. Kölmel, *Chem. Phys. Lett.*, 1989, **162**, 165–169; O. Treutler and R. Ahlrichs, *J. Chem. Phys.*, 1995, **102**, 346–354; K. Eichkorn, O. Treutler, H. Öhm, M. Häser and R. Ahlrichs, *Chem. Phys. Lett.*, 1995, **242**, 652–660.
33. A. D. Becke, *J. Chem. Phys.*, 1993, **98**, 5648–5652; A. D. Becke, *Phys. Rev. A*, 1988, **38**, 3098–3100; C. Lee, W. Yang and R. G. Parr, *Phys. Rev. B*, 1988, **37**, 785–789.
34. A. Schäfer, C. Huber and R. Ahlrichs, *J. Chem. Phys.*, 1994, **100**, 5829–5835.
35. A. J. Wachters, *J. Chem. Phys.*, 1970, **52**, 1033–1036.
36. P. Deglmann, F. Furche and R. Ahlrichs, *Chem. Phys. Lett.*, 2002, **362**, 511–518.
37. A. P. Scott and L. Radom, *J. Phys. Chem.*, 1996, **100**, 16502–16513; M. D. Halls, J. Velkovski and H. B. Schlegel, *Theor. Chem. Acc.*, 2001, **105**, 413–421.
38. K. R. Asmis, G. Meijer, M. Brümmer, C. Kaposta, G. Santambrogio, L. Wöste and J. Sauer, *J. Chem. Phys.*, 2004, **120**, 6461–6470.
39. M. Sierka, J. Döbler, J. Sauer, G. Santambrogio, M. Brümmer, L. Wöste, E. Janssens, G. Meijer and K. R. Asmis, *Angew. Chem., Int. Ed.*, 2007, **46**, 3372–3375.
40. D. M. Deaven and K. M. Ho, *Phys. Rev. Lett.*, 1995, **75**, 288–291.
41. F. Weigend and R. Ahlrichs, *Phys. Chem. Chem. Phys.*, 2005, **7**, 3297–3305.
42. M. J. O. Deegan and P. J. Knowles, *Chem. Phys. Lett.*, 1994, **227**, 321–326; C. Hampel, K. A. Peterson and H. J. Werner, *Chem. Phys. Lett.*, 1992, **190**, 1–12.
43. H.-J. Werner, P. J. Knowles, R. Lindh, F. R. Manby, P. C. M. Schütz, T. Korona, G. Rauhut, R. D. Amos, A. Bernhardsson, A. Berning, D. L. Cooper, M. J. O. Deegan, A. J. Dobbyn, F. Eckert, C. Hampel, G. Hetzer, A. W. Lloyd, S. J. McNicholas, W. Meyer, M. E. Mura, A. Nicklaß, P. Palmieri, R. Pitzer, U. Schumann, H. Stoll, A. J. Stone, R. Tarroni and T. Thorsteinsson, MOLPRO package of *ab initio* programs, 2006.
44. P. J. Knowles, C. Hampel and H. J. Werner, *J. Chem. Phys.*, 1993, **99**, 5219–5227.
45. J. D. Watts, J. Gauss and R. J. Bartlett, *J. Chem. Phys.*, 1993, **98**, 8718–8733; J. Gauss, W. J. Lauderdale, J. F. Stanton, J. D. Watts and R. J. Bartlett, *Chem. Phys. Lett.*, 1991, **182**, 207–215.
46. J. F. Stanton, J. Gauss, J. D. Watts, P. G. Szalay and R. J. Bartlett, ACES II, Mainz–Austin–Budapest, 2006.
47. M. F. Manning, *J. Chem. Phys.*, 1935, **3**, 136–138.
48. D. W. Arnold, PhD Thesis, University of California at Berkeley, 1994.
49. B. Tepper, B. Richter, A. C. Dupuis, H. Kühlenbeck, C. Hucho, P. Schilbe, M. A. bin Yarmo and H.-J. Freund, *Surf. Sci.*, 2002, **496**, 64–72.
50. H.-J. Zhai, J. Döbler, J. Sauer and L.-S. Wang, *J. Am. Chem. Soc.*, 2007, **129**, 13270–13276.
51. C. D. Sherrill, M. S. Lee and M. Head-Gordon, *Chem. Phys. Lett.*, 1999, **302**, 425–430; M. Sodupe, J. Bertran, L. Rodriguez-Santiago and E. J. Baerends, *J. Phys. Chem. A*, 1999, **103**, 166–170.
52. G. Pacchioni, F. Frigoli, D. Ricci and J. A. Weil, *Phys. Rev. B*, 2001, **63**, 054102; X. Solans-Monfort, V. Branchadell, M. Sodupe, M. Sierka and J. Sauer, *J. Chem. Phys.*, 2004, **121**, 6034–6041.
53. Z. Y. Chen and J. L. Yang, *Chin. J. Chem. Phys.*, 2006, **19**, 391–394.
54. K. Hermann and M. Witko, in *The Chemical Physics of Solid Surfaces*, ed. D. P. Woodruff, Elsevier, Amsterdam, 2001, vol. 9, pp. 136–198.